Remote Sensing of Environment 149 (2014) 88–99

Contents lists available at ScienceDirect

Remote Sensing of Environment

journal homepage: www.elsevier.com/locate/rse

Evaluation of broadband surface solar irradiance derived from the Ozone Monitoring Instrument

P. Wang [a,b,*], M. Sneep [b], J.P. Veefkind [a,b], P. Stammes [b], P.F. Levelt [a,b]

[a] Faculty of Civil Engineering and Geosciences, Delft University of Technology, P.O. Box 5048, 2600 GA Delft, Netherlands
[b] Royal Netherlands Meteorological Institute (KNMI), P.O. Box 201, 3730 AE De Bilt, Netherlands

ARTICLE INFO

Article history:
Received 13 December 2013
Received in revised form 28 March 2014
Accepted 29 March 2014
Available online 3 May 2014

Keywords:
Broadband surface solar irradiance
Ozone Monitoring Instrument (OMI)
Validation
Baseline Surface Radiation Network (BSRN)
CERES shortwave flux
ISCCP radiation product
OMI effective cloud fraction

ABSTRACT

Surface solar irradiance (SSI) data are important for planning and estimating the production of solar power plants. Long-term high quality surface solar radiation data are needed for monitoring climate change. This paper presents a new surface solar irradiance dataset, the broadband (0.2–4 μm) surface solar irradiance product derived from the Ozone Monitoring Instrument (OMI). The OMI SSI algorithm is based on the Heliosat method and uses the OMI O_2–O_2 cloud product as main input. The OMI SSI data are validated against the globally distributed Baseline Surface Radiation Network (BSRN) measurements at 19 stations for the year 2008. Furthermore, the monthly mean OMI SSI data are compared to independent surface solar irradiance products from International Satellite Cloud Climatology Project Flux Data (ISCCP-FD) and Clouds and the Earth's Radiant Energy System (CERES) data for the year 2005. The mean difference between OMI SSI and BSRN global (direct + diffuse) irradiances is −1.2 W m^{-2} (−0.2%), the root mean square error is 100.1 W m^{-2} (18.1%), and the mean absolute error is 67.8 W m^{-2} (12.2%). The differences between OMI SSI and BSRN global irradiances are smaller over continental and coastal sites and larger over deserts and islands. OMI SSI has a good agreement with the CERES shortwave (SW) model B surface downward flux (SDF) product. The correlation coefficient and index of agreement between monthly mean 1-degree gridded OMI SSI and CERES SW SDF are >0.99. OMI SSI is lower than CERES SW SDF which is partly due to the solar zenith angle. On average, OMI SSI is 13.5 W m^{-2} (2.5%) lower than the ISCCP-FD SW surface downward flux and the correlation coefficient and index of agreement are >0.98 for every month.

1. Introduction

Solar energy is a renewable energy resource and solar power plants will play an important role to meet the world energy demand. The output of a photovoltaic (PV) solar power plant depends on the efficiency of converting solar irradiance into electricity. In recent years, the development of PV techniques and the market for solar energy has grown rapidly (Razykov et al., 2011). In contrast to traditional power plants, the output of a PV plant varies constantly because of the changing solar position during the day and clouds. These impacts have to be taken into account during the planning and operating of a PV plant. Therefore, surface solar irradiance data are important in almost all the phases of a PV power plant, for example, identifying the location, operating the PV system, monitoring the performance, and forecasting the electricity output (Angelis-Dimakis et al., 2011; Kleissl, 2013). Furthermore, surface solar irradiance is an important component in the surface energy balance and a relevant variable in weather prediction and climate models. Long-term global surface solar irradiance products can be used to validate climatological models and monitor climate changes.

In addition to ground-based observations, surface solar irradiance can be derived from satellite measurements by employing either accurate radiative transfer calculations or parameterised empirical relations. An empirical method, called the Heliosat method, was applied to derive the surface solar irradiance product from Meteosat images (Cano et al., 1986). Various versions of this method have been used to generate surface solar radiation datasets, in order to provide solar energy service and support the solar energy community for effectively employing solar energy (http://www.helioclim.org/index.html; http://www.heliosat3.de/home.html). The Heliosat method uses an empirical relationship between cloudy and clear-sky surface solar irradiances, which makes the algorithm fast, robust and suitable for the operational processing of near real-time satellite data (e.g. Hammer et al., 2003; Lefèvre, Wald, & Diabaté, 2007; Rigollier, Levefre, & Wald, 2004). The datasets generated using the Heliosat algorithms are popular in the estimation of PV output (Drews, Beyer, & Rindelhardt, 2008). At the same time, the Heliosat algorithms and datasets have undergone extensive validations (e.g. Hollmann, Mueller, & Gratzki, 2006; Mueller et al., 2004, Mueller, Matsoukas, Gratzki, Hollmann, & Behr, 2009; Perez et al.,

* Corresponding author.
E-mail address: Ping.Wang@knmi.nl (P. Wang).

http://dx.doi.org/10.1016/j.rse.2014.03.036

2001, Perez, Seals, & Zelenka, 1997; Zelenka, Perez, Seals, & Reme, 1999).

Modified Heliosat algorithms have been applied to make surface solar irradiance products from both geostationary satellite measurements and from polar-orbiting satellite measurements. For example, a CM-SAF (Climate Monitoring Satellite Application Facility) surface solar irradiance time series (1983–2005) has been derived from the Meteosat geostationary satellites (Posselt, Mueller, Stöckli, & Trentmann, 2012). Near real-time and monthly mean gridded SSI products from 2002 to 2012 were derived from SCIAMACHY (SCanning Imaging Absorption spectroMeter for Atmospheric ChartographY) on board of the polar orbiting Envisat (Bovensmann et al., 1999; Wang, Stammes, & Mueller, 2011). In principle, the cloud index in the Heliosat method is comparable to the effective cloud fraction derived from the FRESCO (Fast Retrieval Scheme for Clouds from the Oxygen A band) algorithm (Koelemeijer, Stammes, Hovenier, & de Haan, 2001; Wang, Stammes, van der A, Pinardi, & van Roozendael, 2008). Therefore, the FRESCO SSI algorithm was developed according to the Heliosat empirical equations but using the effective cloud fraction to compute SSI (Wang et al., 2011). The FRESCO SSI algorithm has been applied to SCIAMACHY measurements and the SCIAMACHY FRESCO cloud and SSI level 2 products are available on the TEMIS web site (http://www.temis.nl). The monthly mean gridded cloud and SSI products are available in the KNMI Climate Explorer (http://climexp.knmi.nl/).

The Ozone Monitoring Instrument (OMI) is an Ultraviolet/Visible (UV/VIS) spectrometer on board the EOS-Aura spacecraft, launched in July 2004 (Levelt et al., 2006). OMI provides daily global coverage with a spatial resolution of 13 km × 24 km. The equator overpass time of Aura is 13:45 local time (LT). Atmospheric composition, for example ozone, nitrogen dioxide and sulphur dioxide, is derived from the UV/VIS spectra. Cloud and aerosol properties are also retrieved from OMI because they are required in the atmospheric composition retrievals. OMI is a heritage of GOME (Global Ozone Monitoring Experiment), SCIAMACHY and TOMS (Total Ozone Mapping Spectrometer). Because the wavelength range of OMI does not cover the oxygen A band (755–775 nm), the FRESCO algorithm cannot be applied to the OMI measurements. Instead, the effective cloud fraction and cloud pressure products are derived from the O_2–O_2 absorption band at 477 nm. Therefore, similar to the SCIAMACHY SSI product, the OMI SSI product can be derived from the O_2–O_2 effective cloud fraction (Acarreta, de Haan, & Stammes, 2004).

In this paper, we will give a short description of the OMI SSI algorithm in Section 2. The validation and inter-comparison datasets are described in Section 3. The results for the validation and comparisons are presented in Section 4. Conclusions are drawn in Section 5.

2. OMI SSI algorithm

The OMI SSI algorithm follows the principle of the Heliosat method and employs the Heliosat empirical equations to convert the cloud index into the transmittance at the surface. A Heliosat algorithm usually has three steps: first calculate the cloud index; then calculate the clear-sky surface solar irradiance using a radiative transfer model; finally, calculate the full-sky surface solar irradiance from the clear-sky surface solar irradiance and the cloud index. The cloud index characterises the reflective properties of the atmosphere and is usually calculated using the reflectance of the visible channel (e.g. from Meteosat). In the cloud index calculation, the upper boundary of the cloud reflectance (albedo) is chosen from the brightest clouds or the 95–98 percentile of the maximum value. The effective cloud fraction can be calculated using the same formula as the cloud index (Wang et al., 2011). In the OMI SSI algorithm, the cloud index is replaced by the effective cloud fraction derived from the O_2–O_2 absorption band centred at 477 nm (Acarreta et al., 2004; Sneep et al., 2008). The OMI O_2–O_2 effective cloud fraction is determined from a fit of the simulated reflectances assuming a Lambertian cloud model with a cloud albedo of 0.8 to the measured TOA reflectances at the continuum wavelengths of the O_2–O_2 absorption band (460–490 nm). Using this setting, the cloud index and O_2–O_2 effective cloud fraction have similar values.

An OMI orbit has a swath width of 2600 km. The viewing zenith angle increases from 0° at nadir to about 70° at the edges of the swath. The O_2–O_2 effective cloud fraction increases from nadir towards the edges of the swath, because clouds appear brighter in pixels with a slant viewing geometry. This feature will cause larger SSI values in nadir and smaller SSI values at the edges of the swath, even if the solar zenith angles (SZA) would be constant across the swath. In fact, the solar zenith angle is smaller at the west side of the swath than at the east side of the swath. Therefore, the O_2–O_2 effective cloud fractions have to be corrected for the cross track pixel dependence (viewing angle dependence) before being used in the SSI calculations. This is the first step of the OMI SSI algorithm. The flowchart of the OMI SSI algorithm is shown in Fig. 1.

The correction of the cross-track pixel dependence is illustrated in Fig. 2. The cross-track pixel dependence of the effective cloud fraction is corrected by using a 2nd-order polynomial fit as a function of cross-track pixel number:

$$c_{\mathrm{eff\_fit}} = a_0 + a_1 x + a_2 x^2, \tag{1}$$

where $c_{\mathrm{eff\_fit}}$ is the fitted effective cloud fraction, x is the cross track pixel number from 6 to 55, $a_0 = 4.22 \times 10^{-1}$, $a_1 = -8.63 \times 10^{-3}$, $a_2 =$

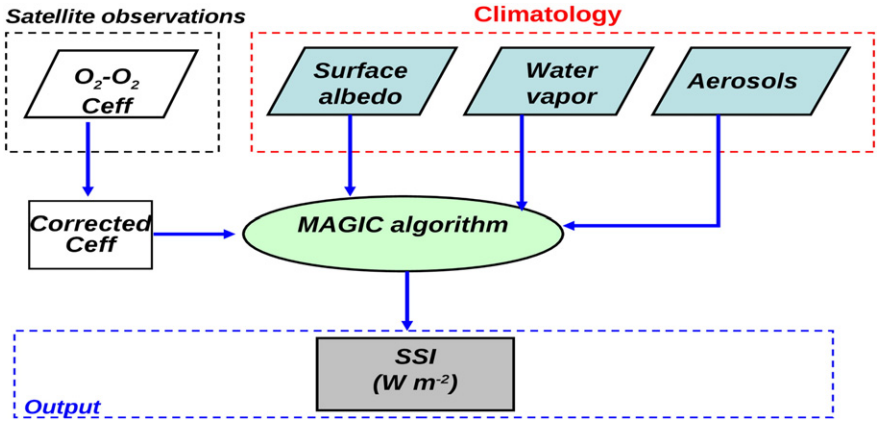

Fig. 1. Flowchart of the OMI SSI algorithm. C_{eff} is effective cloud fraction.

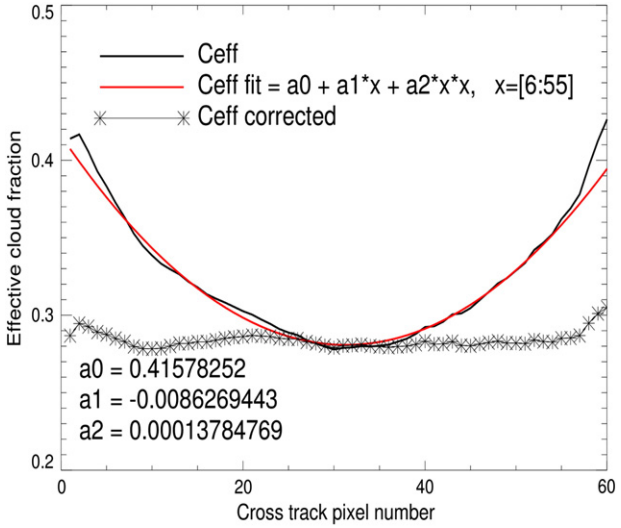

Fig. 2. Correction of the cross-track pixel dependence (viewing angle dependence) of OMI effective cloud fractions. The black line (c_{eff}) is the cross-track mean effective cloud fractions derived from one year of global OMI O_2–O_2 effective cloud fractions in 2005.

1.38×10^{-4}. The corrected effective cloud fraction (c_{eff_corr}) is computed using:

$$c_{eff\_corr} = \frac{<c_{eff}>}{c_{eff\_fit}} * c_{eff}, \quad (2)$$

where c_{eff} is the actual effective cloud fraction, $<c_{eff}>$ is the arithmetic average of c_{eff} from pixel number 25 to 35. The polynomial coefficients (a_0, a_1, a_2) and $<c_{eff}>$ are derived from one year of global O_2–O_2 effective cloud fraction data in 2005.

In the second step, the clear sky irradiance (SSI_{clr}) is computed using the Mesoscale Atmospheric Global Irradiance Code (MAGIC; Mueller et al., 2004, 2009) from 0.2 to 4 μm. The solar constant is 1365 W m^{-2} at a distance of one Astronomical Unit and is corrected with the actual Sun–Earth distance. MAGIC uses monthly climatologies of water vapour, aerosol optical thickness (AOT), aerosol single scattering albedo, and broadband surface albedo data as input in the clear-sky surface solar irradiance calculations. The water vapour climatology is taken from the European Centre for Medium-Range Weather Forecast (ECMWF) reanalysis data ERA Interim at a 0.25° × 0.25° grid. The aerosol optical thickness and single scattering albedo are taken from the Kinne/CM-SAF aerosol climatology at 1° resolution (Kinne et al., 2006). The asymmetry parameter of the aerosol scattering phase function is assumed to be 0.7. The broadband surface albedo climatologies in the MAGIC algorithm consist of the SARB/CERES surface albedo background map and the CERES/IGBP land-use map (http://www-surf.larc.nasa.gov).

Finally, the full-sky surface solar irradiance (SSI) is derived from:

$$SSI = SSI_{clr} * k, \quad (3)$$

where k is called clear-sky index and is related to the effective cloud fraction (c_{eff}) through Eqs. (4)–(7) (Hammer et al., 2003; Rigollier et al., 2004):

$$\text{if } -0.2 < c_{eff} < 0, \quad k = 1.2, \quad (4)$$

$$\text{if } 0 \le c_{eff} \le 0.8, \quad k = 1 - c_{eff}, \quad (5)$$

$$\text{if } 0.8 < c_{eff} \le 1.1, \quad k = 2.0667 - 3.6667 c_{eff} + 1.6667 c_{eff}^2, \quad (6)$$

$$\text{if } 1.1 < c_{eff}, \quad k = 0.05. \quad (7)$$

Eqs. (4)–(7) were derived from collocated ground-based and satellite observations at several sites in Europe and were originally used in the Heliosat-1 algorithm. Because it showed robust and reliable performance in validations, these equations have been used in other versions of the Heliosat algorithm as well (Rigollier et al., 2004).

OMI SSI is a level 2 product (OMI-AURA_L2-OMSSI) processed in near real-time and off-line at KNMI, and is stored in the netCDF format. In this paper, OMI SSI refers to the broadband full-sky surface solar global (direct + diffuse) irradiance in the OMSSI file. The effective cloud fraction, clear-sky index, climatological data of water vapour, aerosols and broadband surface albedo, clear-sky surface solar irradiance, snow/ice extent and other standard L2 data (measurement time, geolocation, sun-satellite geometries, and quality flags) are also provided in the OMSSI file as diagnostic data. The snow/ice extent is used in the OMI O_2–O_2 cloud retrieval algorithm and has large impact on the effective cloud fraction through the surface albedo. The OMI SSI is calculated at sea level (0 km) because the surface elevation is assumed to be 0 in the MAGIC code. The effect of the total ozone column on the broadband surface solar irradiance is relatively small (Mueller et al., 2004). Although the OMI total ozone column data from the DOAS (Differential Optical Absorption Spectroscopy) algorithm are included in the OMSSI files, the total ozone column used in the OMI SSI calculation is a constant of 345 DU.

3. Datasets used for the validation and comparisons

3.1. Baseline Surface Radiation Network (BSRN) data

The BSRN stations provide observations of the best possible quality of short- and long-wave surface radiation fluxes at 1 min sampling rate by using pyranometers and pyroheliometers. The BSRN instruments are regularly maintained and calibrated according to strict requirements (McArthur, 2004; Ohmura et al., 1998). The estimated calibration uncertainties in the shortwave global irradiance are 5 W m^{-2} and the operational uncertainties are typically 14 ± 6 W m^{-2} for direct irradiance and 9 ± 3 W m^{-2} for diffuse irradiance (Shi & Long, 2002). The BSRN sites have different geographic, topographic, and surface type distributions.

The downward shortwave global irradiances (DSGL1) calculated from the pyrheliometer and shaded pyranometer measurements were used to validate the instantaneous (single pixel) OMI SSI data at the BSRN sites. The DSGL1 is considered to be more accurate than the global irradiance measured by the pyranometer (DSGL2), mainly because of the directional error in the measurement of global radiation. The difference between DSGL1 and DSGL2 is monitored in the data quality check (McArthur, 2004). In order to reduce the effect of cloud variations, the measured 1-minute BSRN global irradiances were averaged over 60 min centred at the OMI overpass time (about 13:45 LT).

3.2. CERES SW surface downward flux

The Clouds and the Earth's Radiant Energy System (CERES) is a three-channel radiometer. It measures reflected solar radiation (0.3–5 μm), emitted terrestrial radiation (8–12 μm), and total radiation from 0.3 μm to beyond 100 μm with a spatial resolution of 20 km at nadir (Wielicki et al., 1996). There are two CERES instruments on board the Aqua spacecraft which flies about 10 min ahead of the Aura spacecraft in the 'A-Train' satellite constellation. In this analysis, we used the SW surface downward flux computed using SW model B in the SSF (Single Scan Footprint) Edition 3A product for Aqua (CERES Aqua FM3 Edition 3A SSF).

The CERES SW model B utilises the Langley Parameterised Shortwave Algorithm (LPSA) and employs a parameterised radiative transfer model to estimate SW radiation at the surface for both clear-sky and full-sky conditions (Darnell, Staylor, Gupta, Ritchey, & Wilber, 1992; Gupta, Kratz, Stackhouse, & Wilber, 2001). The cloud information comes from the MODIS instrument (Moderate Resolution Imaging Spectroradiometer) on board Aqua. The LPSA algorithm has gone through extensive validations and the Edition 3A SW surface flux product has also been validated using ground-based measurements (Kratz, Gupta, Wilber, & Sothcott, 2010; Yan, Huang, Minnis, Wang, & Bi, 2011; CERES Aqua Edition 3A SSF Surface Fluxes — Accuracy and Validation, https://eosweb.larc.nasa.gov/sites/default/files/project/ceres/quality_summaries/ssf_surface_flux_aqua_ed3A.pdf). According to the validations, generally, the Aqua SW surface flux product is lower than the ground-based measurements for clear-sky cases and higher than the ground-based measurements for cloudy cases. Because the overpass time of Aqua and Aura is very close and the complexity of the SW model B (LPSA algorithm) is comparable to the OMI SSI algorithm, this gives us a unique opportunity to compare these two products directly.

3.3. ISCCP FD shortwave flux

ISCCP-FD is a 25-year (1983–2007) global radiative flux dataset produced by the International Satellite Cloud Climatology Project (ISCCP) (Zhang, Rossow, Lacis, Oinas, & Mishchenko, 2004, Zhang, Rossow, & Stackhouse, 2006). It provides the all-sky (full-sky) and clear-sky, upwards and downwards, shortwave and longwave radiative fluxes at 5 levels (surface (SRF), 680 hPa, 440 hPa, 100 hPa and top-of-atmosphere). All products are reported with a resolution of 3 h and 280 km (equal-area map equivalent to 2.5° latitude–longitude at the equator). The overall uncertainty of the ISCCP-FD SRF product is estimated to be 10–15 W m^{-2}, according to the evaluations using Earth Radiation Budget Experiment (ERBE), CERES and BSRN data (Zhang et al., 2004).

The ISCCP-FD product was created by employing the NASA GISS climate Global Circulation Model (GCM) radiative transfer code and a collection of global datasets describing the properties of the clouds and the surface every 3 h (ISCCP cloud product); daily atmospheric temperature and humidity profiles; climatology of cloud vertical layer distribution and particle size, and other important variables. The radiative transfer simulation and cloud information are more detailed and complex than those in the OMI SSI algorithm. Therefore, ISCCP-FD is an independent product to compare with OMI SSI. In the comparison we used the 3-hourly, daily ISCCP-FD shortwave surface flux product (SW SRF) at 2.5° × 2.5° (latitude × longitude) grid.

4. Results

4.1. OMI SSI product

An example of the OMI SSI product for 1 January 2005 is shown in Fig. 3. The missing data at high latitudes are due to the solar zenith angle (SZA) being greater than 88°. In order to separate each orbit, the first and last pixels in a swath were not plotted. The SSI map reflects the latitudinal gradient of SSI due to the SZA dependence and the reduction of SSI caused by clouds. In each orbit, the SSI values in the west are often larger than those in the east because the SZA increases from west to east in an OMI orbit. The low SSI regions which appear as north–south oriented stripes at the middle-left of some swaths are caused by sun glint which often occurs on tropical ocean surfaces. In cloud-free scenes, the sun glint on the ocean surface may increase the (apparent) effective cloud fraction to about 0.2. Because of this positive bias on the effective cloud fraction, OMI SSI has a small negative bias for the sun glint contaminated pixels. The effective cloud fraction is corrected for the cross-track pixel dependence in the OMI SSI product. Fig. 4 shows the effective cloud fraction data on 1 January, 2005 before and after the correction.

The OMI SSI product is derived for every OMI pixel having an effective cloud fraction value, which includes pixels covered by snow/ice. Because the effective cloud fraction derived from the O_2–O_2 algorithm is less accurate over snow and ice surface, the OMI SSI data over snow/ice contaminated pixels are excluded in the evaluation. During summer in Polar Regions, it is possible to have daytime measurements from the descending orbits (usually in the darkness). In this paper, the OMI SSI data in the descending orbits are excluded; only ascending orbits are used.

4.2. Validation using the BSRN data

The OMI SSI data were validated against one year of BSRN data at 19 sites in 2008. The surface types of the sites include continent, coast, island, and desert. The geolocations and heights of the sites are presented in Table 1. A detailed description of the BSRN stations is on the website, http://www.bsrn.awi.de/en/stations/listings/. The statistical analyses were performed for every single site and for all the surface types. The OMI SSI data impacted by the row anomaly were removed from the dataset. The row anomaly started on 25 June 2007 at row 53 and 54. Since 11 May 2008 the cross-track position 37–42 are affected towards the northern end of the OMI orbit (so part of the orbit) (http://www.knmi.nl/omi/research/product/). Not much data are impacted by the row anomaly in 2008. We got 5651 collocated data points, on average

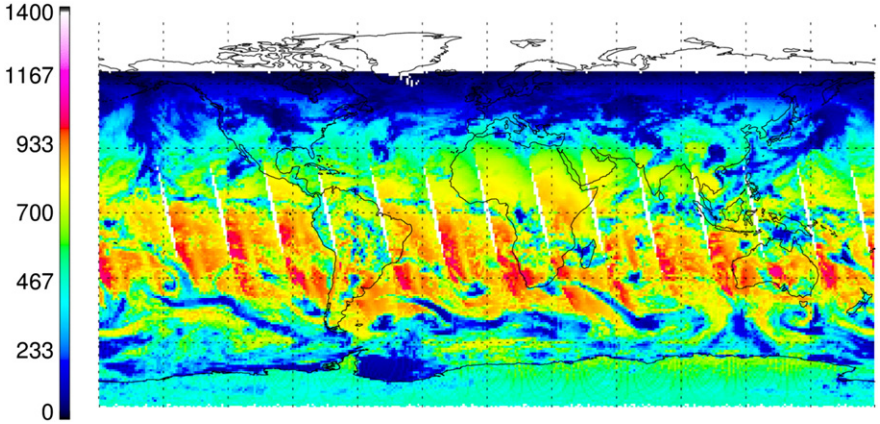

Fig. 3. An example of OMI daily surface solar irradiance map for 1 January 2005. The daily SSI map consists of 15 OMI orbits. Unit: W m^{-2}. SZA < 88°.

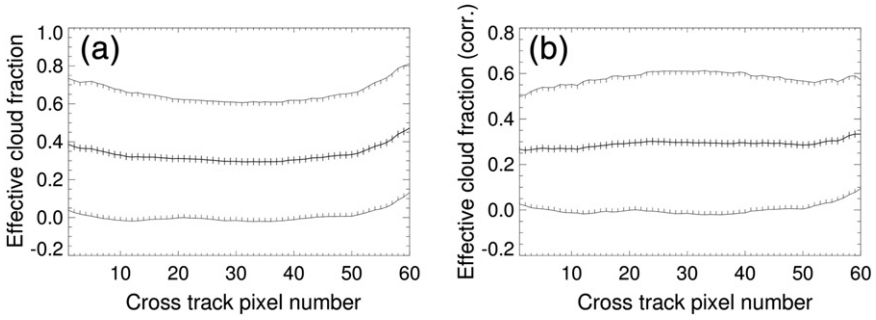

Fig. 4. OMI cross-track mean effective cloud fractions with one sigma standard deviation for 1 January 2005: (a) original data, (b) corrected for the cross-track pixel (viewing angle) dependence.

about 300 data per site. The statistical results, such as mean, bias, root mean square error (RMSE), mean absolute error (MAE), correlation coefficient and index of agreement are given in Tables 1 and 2 per site and per surface type, respectively. The RMSE is more sensitive to outliers than the MAE, so in this paper both errors are provided. It is pointed out by Willmott (1982) that the Pearson's correlation coefficient is often inappropriate or misleading when used to compare model-predicted (retrieved) and observed variables. Therefore, the index of agreement (d) is calculated using the equation proposed by Willmott (1982):

$$d = 1 - \frac{\sum_{i=1}^{n} (P_i - O_i)^2}{\sum_{i=1}^{n} \left(|P_i - \overline{O}| + |O_i - \overline{O}| \right)^2}, \quad 0 \le d \le 1, \tag{8}$$

where O are observations, P are model retrieved or predicted variables, and n is the number of elements in P and O. A large d value suggests that the model retrievals are close to the observations.

Fig. 5 shows the scatter plot of OMI SSI versus BSRN global irradiance for every site.

A good linear correlation was found for every site, whilst the bias varied from −32.9 to +32.1 W m^{-2} (−4% to +6%), the root mean square error varied from 69 to 153 W m^{-2}. The correlation coefficient and index of agreement for all the data are 0.936 and 0.967, respectively. As can be seen in Table 1, at six BSRN sites (TOR, CAB, BOS, BIL, CAR, MAN), the bias errors are smaller than 1%, which is a good agreement. At TOR, CAB, BIL and CAR, the RMSE and MAE are about 75 W m^{-2} and 50 W m^{-2}, respectively. However, at the BOS and MAN sites, the RMSE and MAE are much larger than at the other 4 sites and the correlation coefficient and the index of agreement are about 0.1 smaller. This indicates that there are some outliers at the BOS and MAN sites, which is consistent with the scatter plots in Fig. 5. The sites, TOR, CAB, BIL and CAR are all in rural, flat regions, which is favourable for the OMI SSI retrievals. Additionally, the BSRN measurements at these sites could be more representative for the surrounding area (Hakuba, Folini, Sanchez-Lorenzo, & Wild, 2013). Because OMI SSI is calculated at 0 m, OMI SSI should be underestimated at the BOS site (elevation of 1689 m). However, the bias of −2.2 W m^{-2} is too small to explain the altitude effect. The correlation coefficient is relatively low, 0.854, at BOS. Over mountainous area, the surface height and surface albedo may have large variations in one OMI pixel, which can cause large uncertainties in the effective cloud fraction. We suspect that the effective

Table 1
OMI SSI validation results using the BSRN global irradiances at 19 stations in 2008. Elev. = Elevation of the BSRN station. Bias = OMI SSI–BSRN, RMSE = root mean square error, MAE = mean absolute error, Corr = correlation coefficient. D = index of agreement. The abbreviations of the station names can be found on the BSRN web page, http://www.bsrn.awi.de/en/stations/listings/.

BSRN sites*	Lat °N	Lon °E	Elev. m	OMI SSI W m^{-2}	BSRN W m^{-2}	Bias %	RMSE W m^{-2}	MAE W m^{-2}	Corr.	D
TOR	58.25	26.46	70	286.3	286.5	−0.1	74.7	48.1	0.955	0.977
CAB	51.97	4.93	0	354.5	352.5	0.6	74.9	53.4	0.954	0.976
FPE	48.32	−105.10	634	470.1	483.0	−2.7	94.2	65.5	0.938	0.967
PAY	46.82	6.94	491	493.8	468.0	5.5	105.9	72.5	0.924	0.959
PSU	40.72	−77.93	376	460.5	478.3	−3.7	101.0	73.7	0.936	0.965
BOS	40.13	−105.24	1689	558.0	560.2	−0.4	142.9	99.0	0.854	0.922
BON	40.07	−88.37	213	481.4	502.4	−4.2	114.7	70.9	0.920	0.958
XIA	39.75	116.96	32	582.0	549.9	5.8	82.1	64.3	0.945	0.965
CLH	36.91	−75.71	37	564.9	584.6	−3.4	68.9	50.9	0.973	0.984
BIL	36.61	−97.52	317	596.7	596.4	0.1	76.0	49.3	0.959	0.979
TAT	36.05	140.13	25	485.5	472.6	2.7	89.4	60.7	0.936	0.966
GCR	34.25	−89.87	98	552.7	563.9	−2.0	82.9	60.3	0.958	0.977
BER	32.27	−64.67	8	602.0	581.3	3.6	128.6	84.8	0.873	0.931
SBO	30.91	34.78	500	730.1	763.0	−4.3	72.5	55.5	0.959	0.968
TAM	22.78	5.51	1385	776.6	801.1	−3.1	97.6	68.9	0.898	0.935
KWA	8.72	167.73	10	710.6	692.7	2.6	93.3	65.2	0.889	0.940
CAR	4.08	5.06	100	509.6	513.6	−0.8	72.4	47.4	0.964	0.982
MAN	2.06	147.43	6	612.0	606.8	0.9	152.5	115.6	0.819	0.898
COC	−12.19	96.84	–	691.1	664.1	4.1	123.8	85.1	0.846	0.907
All sites				553.1	554.2	−0.2	100.1	67.8	0.936	0.967

* Island surface type includes KWA, MAN and COC sites. Coastal surface type includes BER and TAT sites. Desert surface type consists of TAM and SBO sites. The rest belongs to the continental surface type.

Table 2
Similar to Table 1 but the BSRN stations are grouped according to surface type. N: number of data points. Bias = OMI SSI–BSRN, RMSE = root mean square error, MAE = mean absolute error, Corr = correlation coefficient, D = index of agreement.

Surface type	N	OMI SSI W m^{-2}	BSRN W m^{-2}	Bias %	RMSE W m^{-2}	MAE W m^{-2}	Corr.	D
Continental	3258	484.3	486.5	−0.5	95.2	63.8	0.942	0.970
Coastal	608	524.7	527.8	−0.6	80.0	55.9	0.956	0.977
Island	1155	652.7	635.2	2.8	126.8	88.2	0.857	0.921
Desert	630	753.6	782.2	−3.7	86.1	62.2	0.930	0.953

cloud fraction has a larger uncertainty for this mountainous site. The BSRN measurements at a mountainous site are generally less representative for a large area, say the OMI pixel size (Hakuba et al., 2013).

Table 2 shows that the OMI SSI is more accurate at continental, coastal and desert sites than at island sites. MAN, COC and KWA are tropical island sites, which have large RMSE, MAE and relatively small correlation coefficient and index of agreement. The error may also be related to the surface albedo, because of the mixture of land and ocean in one OMI pixel. Over these island sites, the BSRN data have larger variations because of clouds. This also makes the comparison with OMI measurements more challenging. Generally, over desert sites the RMSE and MAE are small because of fewer clouds and smaller cloud variations. OMI SSI tends to have a smaller bias than the CERES SSF Edition 3A model B SW surface downward flux over continental, coastal, and island surface types. The RMSE of OMI SSI for the four surface types are between 11.0% and 20.0%, which is slightly larger than the CERES validation result of from 10.2% to 16.0% (CERES Aqua Edition 3A SSF Surface Fluxes — Accuracy and Validation, https://eosweb.larc.nasa.gov/sites/default/files/project/ceres/quality_summaries/ssf_surface_flux_aqua_ed3A.pdf).

The OMI SSI values are slightly lower than the BSRN data, especially when BSRN global irradiances are higher than 900 W m^{-2} (see SBO and TAM sites in Fig. 5). This could be partly explained by the 3-dimensional cloud effects (Yan et al., 2011). The high global irradiance values (>900 W m^{-2}) suggest low cloud cover fractions in the scenes. For almost cloud-free scenes, the effective cloud fractions could have relatively large uncertainties due to the surface albedo climatology. The mean difference between OMI SSI and the BSRN global irradiances is −1.2 W m^{-2} (−0.2%) with a RMSE of 100.1 W m^{-2} (18.1%) and a MAE of 67.8 W m^{-2} (12.2%). This result is comparable to the validation

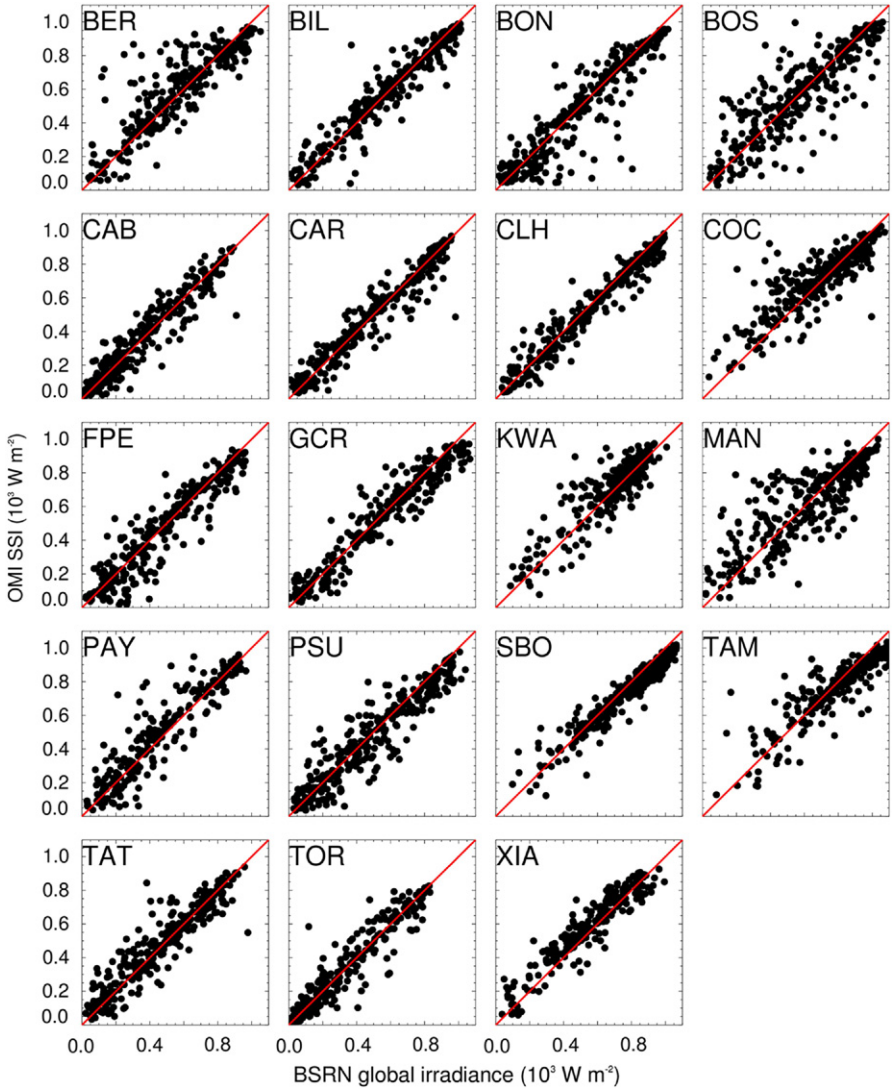

Fig. 5. Scatter plots of OMI SSI versus the hourly mean BSRN global irradiances for every site in 2008. The red lines indicate the one-to-one lines.

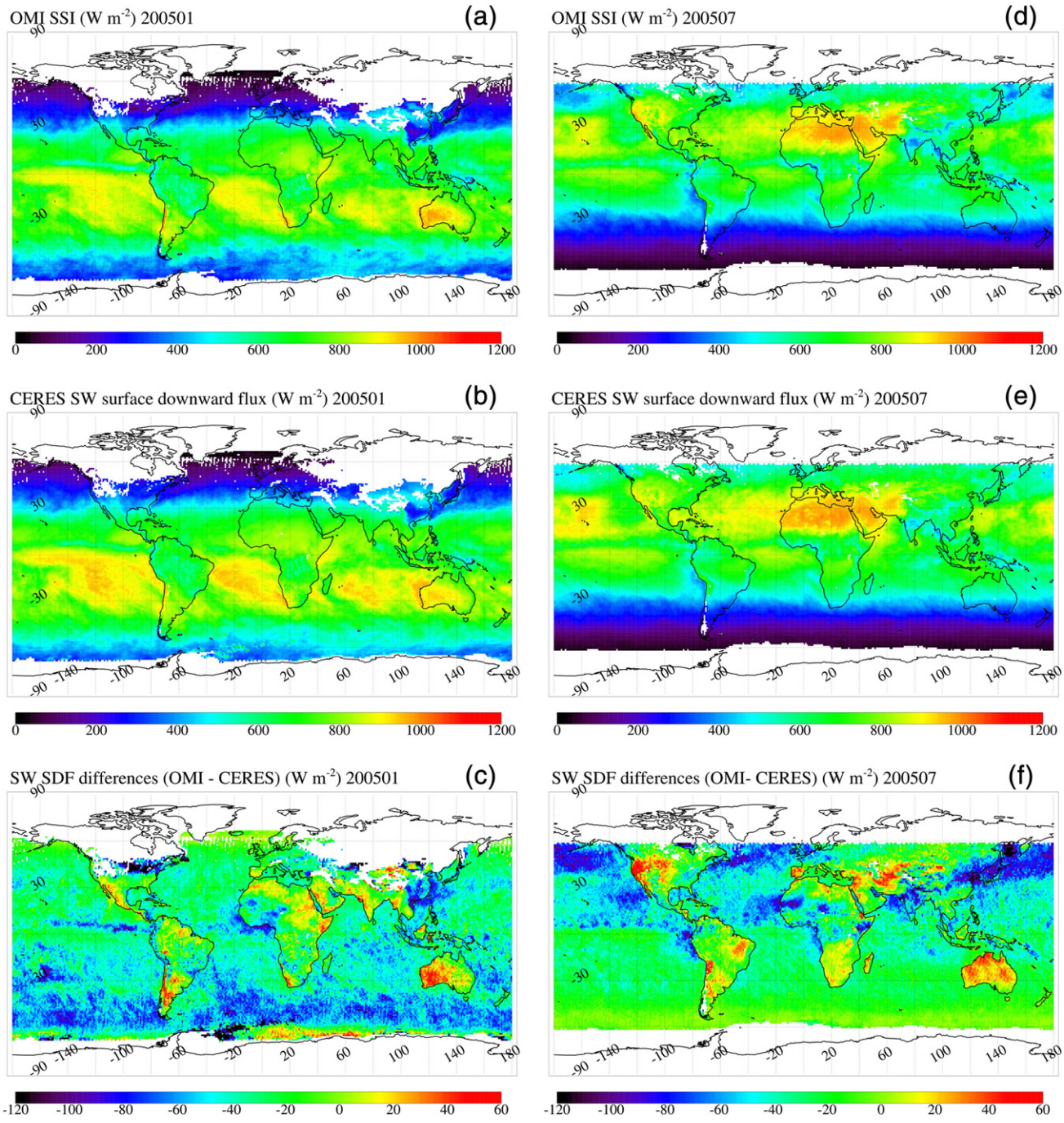

Fig. 6. Monthly mean maps of (a, d) OMI SSI, (b, e) CERES shortwave surface downward fluxes, and (c, f) the differences (OMI–CERES) for January and July 2005.

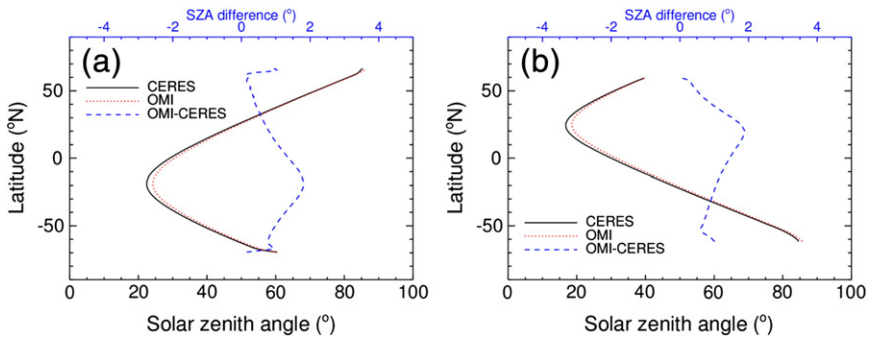

Fig. 7. Zonal mean solar zenith angles (SZA) for CERES and OMI monthly mean gridded data at 1-degree resolution and the SZA differences for (a) January and (b) July 2005.

of SCIAMACHY SSI using the BSRN data (Wang et al., 2011). For SCIAMACHY SSI, the mean difference was -4 W m^{-2} (-1%) and the standard deviation was 101 W m^{-2} (20%).

4.3. Comparison with CERES SW model B surface downward flux

The OMI SSI monthly mean gridded data at 1° × 1° (latitude × longitude) were compared to CERES SSF SW model B surface downward flux (SDF) at the same grid resolution for January and July 2005. In this paper, the monthly mean of OMI SSI is a monthly mean of OMI daily measurements at about 1345 LT. Similarly, the monthly mean of CERES SW SDF is also the monthly mean of CERES daily measurements at about 1335 LT. The pixels having snow/ice on the surfaces were removed according to the snow/ice flags in the OMI SSI level 2 data. Because Aqua flies 10 min ahead of Aura, in every grid box, the SZA is expected to be smaller at the CERES overpass time than at the OMI overpass time. In the comparison, the grid boxes where the CERES SZA was greater than the OMI SZA were removed, which mainly removed the CERES and OMI measurements from about 60°N to 90°N in July. The data between 60°S and 90°S were already removed because of snow/ice on the surface.

OMI SSI, CERES SW surface downward fluxes (SDF), and the difference maps for January and July 2005 are shown in Fig. 6. The OMI SSI and CERES SW SDF maps have very similar features. In January, the smallest solar zenith angles are around 20°S (see Fig. 7a); therefore, the largest surface solar irradiances occur between 0 and 30°S. In July, the largest SSI values occur between 0 and 30°N due to the shift of SZA (see Fig. 7b). As shown in Fig. 7, the zonal means of the SZA differences between OMI and CERES are 0–2°.

Fig. 6(c, f) shows that the differences between OMI SSI and CERES SW SDF have a land and ocean dependence. Over ocean, the OMI SSI values are often lower than the CERES SW surface fluxes, particularly, at 30°S–60°S in January and at 30°N–60°N in July. Over land, the differences between OMI and CERES depend on the geolocation: for example, OMI SSI is higher than CERES SW SDF over west Australia and lower than CERES SW SDF over east China. The land/ocean dependent features suggest that the cause is the differences in the AOT climatologies used in the OMI SSI and CERES model B SW algorithms. The AOT climatology used in the OMI SSI algorithm is shown in Fig. 8 for January and July. The CERES SW model B algorithm uses AOT from WCP-55 aerosol models which have different AOT over land/ocean and have a latitudinal distribution of AOT over land (Deepak & Gerber, 1983; Gupta et al., 2001). In January, the AOT used in the OMI SSI algorithm is higher than the AOT used in CERES over east China and lower than the CERES AOT over west Australia. Therefore, the surface downward fluxes show corresponding negative and positive differences in the maps at the above locations. In the WCP-55 aerosol models, there is no enhanced AOT over ocean at the west of the Sahara desert due to the transportation of desert dust aerosols. This shows up in Fig. 6(c, f) as negative biases. Similar findings were reported by Kratz et al. (2012). The SW surface flux differences in July (see Fig. 6f) are also consistent with the AOT differences in July.

The scatter density plots of OMI SSI versus CERES SW SDF for January and July 2005 are shown in Fig. 9. The statistical results of the comparison between OMI and CERES data are presented in Table 3. The correlation

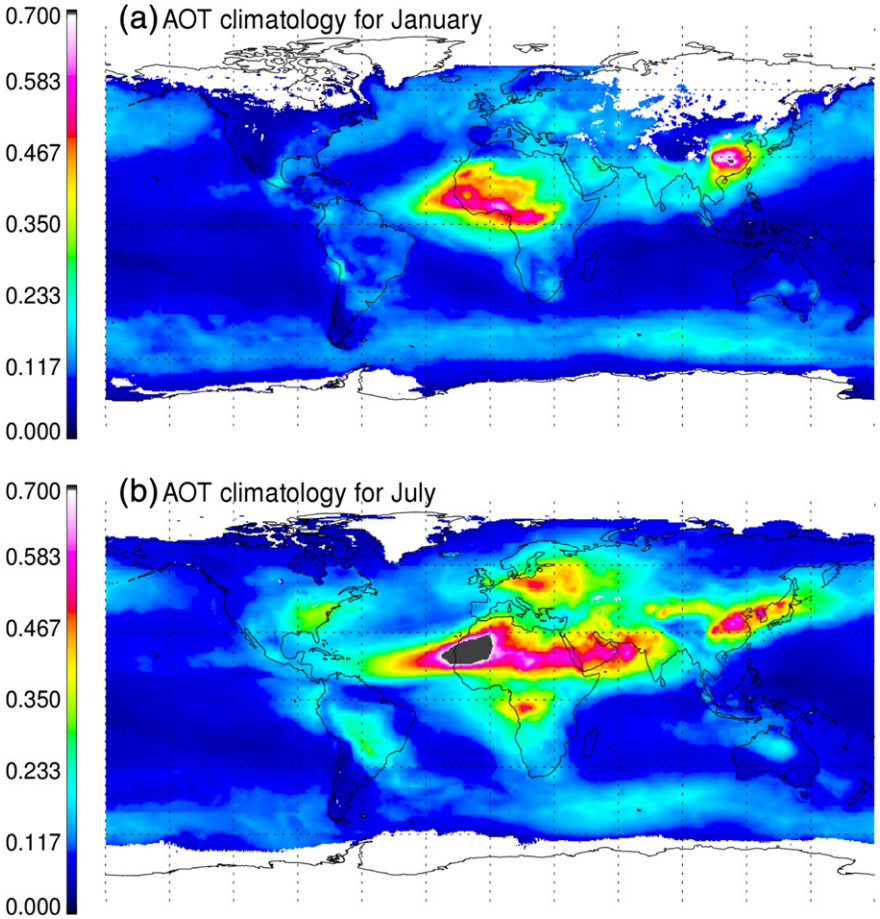

Fig. 8. Aerosol optical thickness climatology used in the OMI SSI algorithm for (a) January and (b) July 2005.

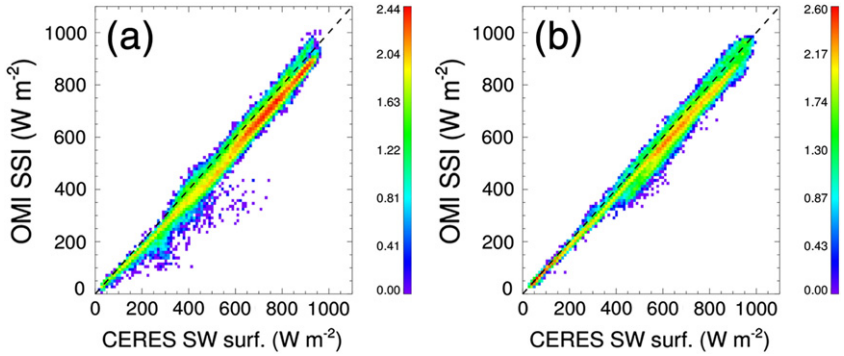

Fig. 9. Scatter density plots of OMI SSI versus CERES shortwave surface downward fluxes (SW SDF) for (a) January and (b) July 2005. The OMI SSI and CERES SW SDF data are monthly mean global data at 1° × 1° grid. Same data as in Fig. 6. The dashed line is the one-to-one line. The colour scale indicates the base-10 logarithm of the number of data points.

Table 3
Statistics for the comparison of OMI SSI with CERES SW surface downward fluxes for monthly mean and daily mean global data in 2005. Bias = OMI SSI–CERES, RMSE = root mean square error, MAE = mean absolute error, Corr. = correlation coefficient, D = index of agreement, SZA = solar zenith angle, SZA diff. = OMI SZA–CERES SZA.

Date	OMI SSI W m^{-2}	CERES W m^{-2}	Bias %	RMSE W m^{-2}	MAE W m^{-2}	Corr.	D	OMI SZA °	SZA diff. °
January	577.0	614.1	−6.0	45.8	39.6	0.992	0.989	41.4	1.1
July	532.5	561.1	−5.1	38.4	31.6	0.995	0.994	42.1	1.1

coefficient is greater than 0.99 for every month. The index of agreement is greater than 0.98. This suggests a good agreement between the OMI SSI and CERES SW SDF. The mean differences between OMI SSI and CERES SW SDF are −37.2 and −28.6 W m^{-2} for January and July with standard deviations of 26.8 and 25.7 W m^{-2}, respectively. The RMSEs for January and July are 45.8 and 38.4 W m^{-2}, respectively, which are larger than the standard deviations because of the bias. The differences in SZA between the OMI and CERES observations contribute significantly to the

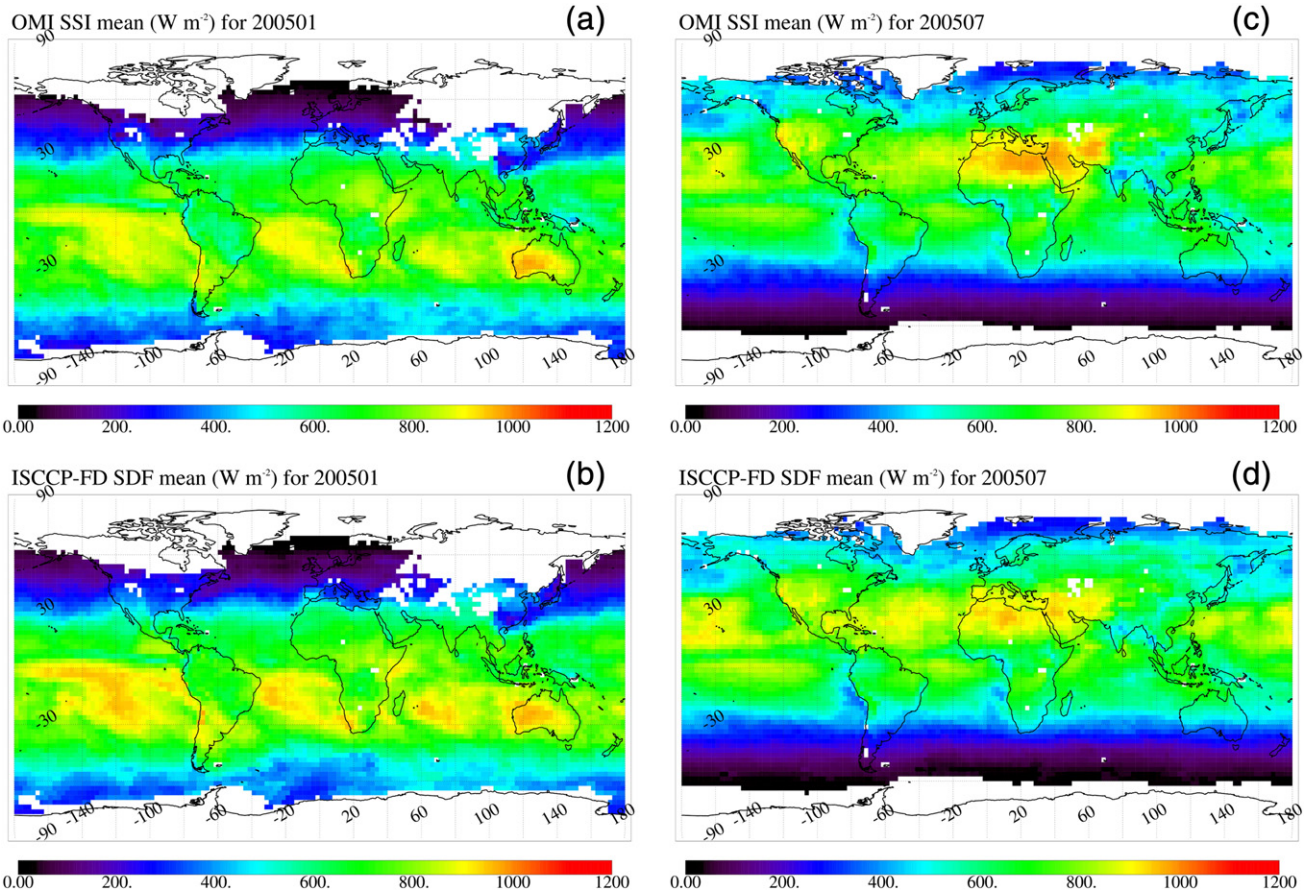

Fig. 10. Monthly mean maps of OMI SSI and ISCCP-FD shortwave surface downward fluxes for (a, b) January 2005 and (c, d) July 2005. The white areas indicate the missing data due to snow/ice at the surface or solar zenith angles of >88°.

flux differences. The global mean SZA difference between OMI and CERES measurements is about 1.2°. A linear fit of OMI SSI versus SZA gives a slope of −12.9 W m^{-2} per degree of SZA for January and −10.6 W m^{-2} per degree of SZA for July. After the correction of the SZA differences between OMI and CERES, the OMI SSI would be 23.0 and 17.0 W m^{-2} lower than CERES SW SDF in January and July, respectively.

Similar to the comparisons of the monthly mean gridded data, daily OMI SSI and CERES SW surface downward fluxes are compared for 1 January and 1 July 2005. The scatter density plots of the daily data are comparable to those of the monthly mean data, except that the scatter is larger. Stammes et al. (2008) have reported that the effective cloud fractions derived from the OMI O_2–O_2 algorithm and MODIS show a high correlation of 0.92 with a very small offset (0.01). The CERES algorithm uses cloud information from MODIS. In an OMI or CERES pixel, the surface solar irradiance is largely determined by the clouds. Consequently, it may be expected that OMI SSI has a good correlation with CERES SW SDF.

4.4. Comparison with ISCCP-FD shortwave surface downward flux (SDF)

Additional to the comparison with CERES data, the OMI SSI data and the ISCCP-FD SW SDF data were compared for monthly mean gridded data at 2.5° × 2.5° (latitude × longitude) grid for one year of data in 2005. The comparison between OMI SSI and CERES SW SDF provides valuable information on the correlation and the detailed structures of these two datasets, but not on the absolute differences because of the different overpass times. In the comparison with the ISCCP-FD data, the ISCCP-FD 3-hourly monthly mean SW surface downward fluxes (SDF) were calculated from the daily 3-hourly ISCCP-FD data and then interpolated at the time (solar zenith angle) of OMI measurements. Therefore, it is possible to examine the absolute differences between OMI SSI and ISCCP-FD SW SDF.

The global maps of OMI SSI and ISSCP-FD SW SDF for January and July 2005 are shown in Fig. 10. OMI SSI and ISCCP-FD SW SDF have similar global features and good agreement. Fig. 11 shows the zonal mean of the clear-sky and full-sky OMI SSI and ISCCP-FD SW SDF data for every month in 2005. The statistics of the comparison is given in Table 4. As shown in Fig. 11, the large differences appear in the tropical regions where the surface solar irradiances are large. The monthly global mean OMI SSI data are 2.7 to 25.8 W m^{-2} (0.5 ~ 4%) lower than the ISCCP-FD SW SDF data for the full-sky scenes (see Table 4). The RMSE is in the range of 33.9 to 55.4 W m^{-2}. However, for the clear-sky scenes, the differences between OMI SSI and ISCCP-FD vary from −7.1 to +3.8 W m^{-2} (−0.95% ~ +0.55%), which are much smaller than for the full-sky scenes. This suggests that the differences between OMI and ISCCP-FD full-sky SSI are mostly caused by clouds. The differences

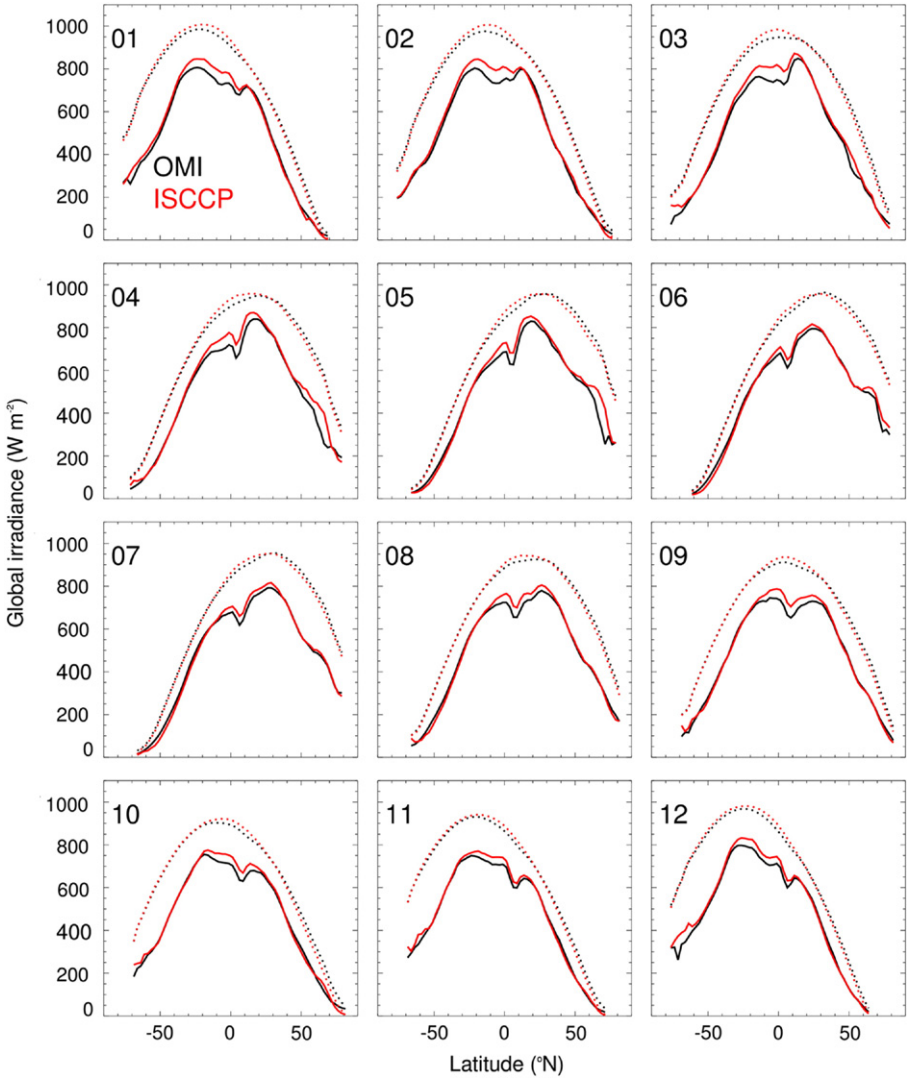

Fig. 11. Zonal means of OMI SSI (black lines) and ISCCP-FD shortwave surface downward fluxes (red lines) for clear-sky and full-sky scenes from January to December 2005. The solid lines show the full-sky irradiances and the dotted lines illustrate the clear-sky irradiances.

Table 4
Monthly mean OMI SSI evaluation results using the ISCCP-FD shortwave surface downward fluxes for 2005. Bias = OMI SSI–ISCCP-FD, RMSE = root mean square error, MAE = mean absolute error, Corr. = correlation coefficient, D = index of agreement, clr = clear-sky.

Month	OMI SSI W m^{-2}	ISCCP W m^{-2}	Bias %	RMSE W m^{-2}	MAE W m^{-2}	Corr.	D	OMI SSI clr W m^{-2}	ISCCP clr W m^{-2}
1	562.0	579.6	−3.0	43.0	34.1	0.987	0.991	762.5	769.4
2	577.1	597.8	−3.5	48.9	36.2	0.982	0.988	777.1	784.1
3	566.4	592.1	−4.4	51.5	35.8	0.982	0.987	757.4	764.7
4	536.7	560.4	−4.2	53.3	34.8	0.980	0.988	712.6	716.8
5	509.8	526.2	−3.1	54.4	33.4	0.979	0.988	679.1	678.4
6	505.6	509.2	−0.7	38.6	28.5	0.989	0.994	674.6	671.3
7	517.1	519.8	−0.5	35.9	28.4	0.990	0.994	684.7	680.9
8	528.2	536.0	−1.5	37.9	29.1	0.988	0.993	701.4	699.6
9	528.5	539.3	−2.0	38.6	29.3	0.987	0.992	697.9	697.8
10	504.8	515.2	−2.0	36.7	28.3	0.988	0.993	677.5	676.4
11	508.2	517.2	−1.7	33.9	26.6	0.991	0.995	686.7	689.5
12	533.7	547.4	−2.5	37.0	28.1	0.990	0.994	723.5	729.5

in the clear-sky simulations could be attributed to aerosols, water vapour, surface albedo, RTM and other variables. The comparisons between the ISCCP-FD and OMI SSI input parameters and the RT codes are beyond this paper.

The scatter density plots of OMI SSI versus ISCCP-FD SW SDF show very good linear correlation between these two products (see Fig. 12). The correlation coefficients are 0.987 and 0.990 for January and July 2005, respectively. Although OMI SSI and ISCCP-FD SW SDF are averaged at a 2.5° × 2.5° resolution, the correlation coefficients are smaller than those between OMI SSI and CERES SW SDF data at 1° resolution. The reason could be that OMI and CERES have a better agreement in the cloud information than OMI and ISCCP.

5. Conclusions

A new broadband surface solar irradiance product has been derived from the OMI O_2–O_2 effective cloud fraction using the Heliosat method. The clear-sky surface solar irradiance is simulated using the MAGIC algorithm. The OMI SSI product is processed in near real-time. According to the validation and comparisons, we may conclude that the OMI SSI product has a similar quality to the CERES SSF Aqua SW model B Edition 3A product and the ISCCP-FD SW surface downward flux product.

The validation against BSRN global irradiance measurements reveals that the OMI SSI is only 1.2 W m^{-2} lower than BSRN data, with a RMSE of 100.1 W m^{-2} (18%). At coastal and continental BSRN sites, OMI SSI is 2 to 3 W m^{-2} lower than the BSRN measurements. For the island surface type, OMI SSI has a positive bias of 18 W m^{-2}. For the desert surface type, OMI SSI has a negative bias of 29 W m^{-2}. The negative bias over desert sites could be due to the three-dimensional effect of clouds. The positive bias over island sites is still not fully understood. It could be due to a bias in the surface albedo databases for the broadband or the O_2–O_2 band. It is interesting to see that the CERES SW model B surface downward flux also has a positive bias over islands and a negative bias over deserts for full-sky conditions, although the validation sites and time periods are different.

OMI SSI has a good linear correlation with the CERES SSF Aqua Edition 3A SW model B downward surface flux product. The correlation coefficient is >0.99 for monthly mean gridded data at 1° grid and >0.98 for daily gridded data at 1° grid. The mean absolute error of OMI SSI is 39.6 W m^{-2} (6.5%) in January and 31.6 W m^{-2} (5.6%) in July 2005, which indicates the consistency of cloud information in these two products. OMI SSI is systematically lower than the CERES SW surface downward flux product, by 6.0% in January and 5.1% in July. This is partly because of the SZA differences: the SZA at OMI overpass time can be a few degrees larger than at CERES overpass time. It is found that the different aerosol climatological data used in the OMI SSI and CERES algorithms can lead to systematic differences between the OMI SSI and CERES SW flux products. In principle, the aerosol climatology used in OMI SSI is newer and more representative for the monthly global aerosol properties than the WCP-55 aerosols used in CERES Edition 3A SW model B. The OMI SSI product would be closer to a new edition of the CERES SW model B surface flux product using better aerosol climatology.

The comparison with the ISCCP-FD SW surface downward flux data gives a global monthly evaluation of the OMI SSI data for 12 months in 2005. OMI SSI is well correlated with ISCCP-FD SW SDF with a correlation coefficient and an index of agreement of >0.98 for every month. Compared to ISCCP-FD SW SDF, OMI SSI has a bias of −13.5 W m^{-2} (2.5%) for full-sky conditions and of −2.0 W m^{-2} for clear-sky conditions. The larger differences appear at tropical regions where the surface

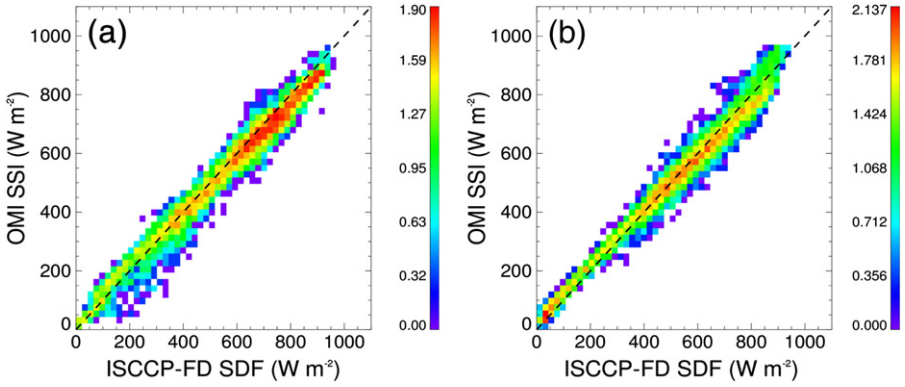

Fig. 12. Scatter density plots of OMI SSI versus ISCCP-FD shortwave surface downward fluxes (SDF) for (a) January and (b) July 2005. The dashed line is the one-to-one line. The colour scale indicates the base-10 logarithm of the number of data points.

SW irradiance is large. This indicates that the O_2–O_2 effective cloud fraction at tropical regions might be too large. The sun glint over ocean could also induce a slightly larger effective cloud fraction and smaller SSI. This has to be evaluated further, because sun glint pixels cannot be exactly detected from the OMI measurements alone.

The OMI SSI product is released as a first version; it can be further improved in many aspects. For example, we have not evaluated the OMI SSI data over snow/ice contaminated pixels. The challenge of sun glint in the SSI product might be solved by using cloud information from Infrared measurements. Actually, the Heliosat method is not limited to the effective cloud fraction derived from the visible wavelengths, although the Heliosat algorithms usually use cloud detection from the visible channel.

Since the effective cloud fraction will also be derived from TROPOMI using the FRESCO algorithm, the SSI algorithm can be a potential TROPOMI product (Veefkind et al., 2012). Because of the relatively small pixel size (7 km × 2 km) of TROPOMI in the O_2 A band, the SSI product will be more specific for a geolocation and would be more suitable for the applications related to solar power plants. For climate research, a long SSI time series from SCIAMACHY to GOME-2, OMI and TROPOMI is foreseen.

Acknowledgements

We would like to thank Dr. Richard Mueller (German weather service; DWD) for the MAGIC code. Robert van Versendaal (KNMI) is acknowledged for processing OMI SSI data. We acknowledge Dr. Wouter H. Knap (KNMI) for the help with BSRN data. We appreciate the BSRN site scientists and Dr. Gert König-Langlo at the BSRN data archive centre for providing high quality data. The BSRN data were downloaded from http://www.bsrn.awi.de/en/home/bsrn/. The ISCCP-FD data were downloaded from http://isccp.giss.nasa.gov/projects/flux.html. We acknowledge the CERES science team for the CERES SW flux product. The CERES data were downloaded from http://ceres.larc.nasa.gov/order_data.php. This research is funded by The Netherlands Space Office (NSO) through the OMI project. We appreciate the two anonymous reviewers for their helpful comments and suggestions.

References

Acarreta, J. R., de Haan, J. F., & Stammes, P. (2004). Cloud pressure retrieval using the O_2–O_2 absorption band at 477 nm. *Journal of Geophysical Research*, *109*, D05204, http://dx.doi.org/10.1029/2003JD003915.

Angelis-Dimakis, A., Biberacher, M., Dominguez, J., Fiorese, G., Gadocha, S., Gnansounou, E., et al. (2011). Methods and tools to evaluate the availability of renewable energy sources. *Renewable and Sustainable Energy Reviews*, *15*, 1182–1200.

Bovensmann, H., Burrows, J. P., Buchwitz, M., Frerick, J., Noël, S., Rozanov, V. V., et al. (1999). SCIAMACHY — Mission objectives and measurement modes. *Journal of Atmospheric Sciences*, *56*(2), 127–150.

Cano, D., Monget, J., Albuisson, M., Guillard, H., Regas, N., & Wald, L. (1986). A method for the determination of the global solar radiation from meteorological satellite data. *Solar Energy*, *37*, 31–39.

Darnell, W., Staylor, F., Gupta, S. K., Ritchey, N. A., & Wilber, A.C. (1992). Seasonal variation of surface radiation budget derived from International Satellite Cloud Climatology Project C1 Data. *Journal of Geophysical Research*, *97*(D14), 15741–15760.

Deepak, A., & Gerber, H. E. (Eds.). (1983). *Report of the experts meeting on aerosols and their climatic effects. WCP-55, Williamsburg, Virginia, 28–30 March 1983* (107 pp.).

Drews, A., Beyer, H. G., & Rindelhardt, U. (2008). Quality of performance assessment of PV plants based on irradiation maps. *Solar Energy*, *82*, 1067–1075.

Gupta, S. K., Kratz, D. P., Stackhouse, P. W., & Wilber, A.C. (2001). *The Langley Parameterized Shortwave Algorithm (LPSA) for surface radiation budget studies version 1.0.* : NASA Langley Research Center, NASA/TP-2001-211272.

Hakuba, M. Z., Folini, D., Sanchez-Lorenzo, A., & Wild, M. (2013). Spatial representativeness of ground-based solar radiation measurements. *Journal of Geophysical Research (Atmosphere)*, *118*, 1–13, http://dx.doi.org/10.1002/jgrd.50673.

Hammer, A., Heinemann, D., Hoyer, C. R. K., Lorenz, E., Mueller, R., & Beyer, H. (2003). Solar energy assessment using remote sensing technologies. *Remote Sensing of Environment*, *86*, 423–432.

Hollmann, R., Mueller, R. W., & Gratzki, A. (2006). CM-SAF surface radiation budget: First results with AVHRR data. *Advance in Space Research*, *37*, 2166–2171.

Kinne, S., Schulz, M., Textor, C., Guibert, S., Balkanski, Y., Bauer, S. E., et al. (2006). An AeroCom initial assessment — Optical properties in aerosol component modules of global models. *Atmospheric Chemistry and Physics*, *6*, 1815–1834, http://dx.doi.org/10.5194/acp-6-1815-2006.

Kleissl, J. (2013). *Solar energy forecasting and resource assessment* (1st ed.). : Academic Press9780123971777.

Koelemeijer, R. B.A., Stammes, P., Hovenier, J. W., & de Haan, J. F. (2001). A fast method for retrieval of cloud parameters using oxygen A band measurements from GOME. *Journal of Geophysical Research*, *106*(D4), 3475–3490, http://dx.doi.org/10.1029/2000JD900657.

Kratz, D. P., Gupta, S. K., Wilber, A.C., & Sothcott, V. E. (2010). Validation of the CERES Edition 2B surface-only flux algorithms. *Journal of Applied Meteorology and Climatology*, *49*, 164–180, http://dx.doi.org/10.1175/2009JAMC2246.1.

Kratz, D. P., Gupta, S. K., Wilber, A.C., Sothcott, V. E., Stackhouse, P. W., & Sawaengphokhai, P. (2012). *Status of the Ed4 surface-only flux algorithm, presentation at the 18th science team meeting* (http://ceres.larc.nasa.gov/order_data.php. http://ceres.larc.nasa.gov/documents/STM/2012-10/Mon_05_CERES18_SOFA.pdf last access date: November, 2013).

Lefèvre, M., Wald, L., & Diabaté, L. (2007). Using reduced data sets ISCCP-B2 from the Meteosat satellites to assess surface solar irradiance. *Solar Energy*, *81*(2), 240–253.

Levelt, P. F., van den Oord, G. H. J., Dobber, M. R., Mälkki, A., Visser, H., de Vries, J., et al. (2006). The ozone monitoring instrument. *IEEE Transactions on Geoscience and Remote Sensing*, *44*(5), 1093–1101, http://dx.doi.org/10.1109/TGRS.2006.872333.

McArthur, L. J. B. (2004). Baseline Surface Radiation Network (BSRN) operations manual — Version 2.1. WMO/TD Rep. 879. Geneva: World Climate Research Programme, World Meteorology Organization.

Mueller, R., Dagestad, K., Ineichen, P., Schroedter-Homscheidt, M., Cros, S., Dumortier, D., et al. (2004). Rethinking satellite based solar irradiance modeling: The SOLIS clear-sky module. *Remote Sensing of Environment*, *91*, 160–174.

Mueller, R., Matsoukas, C., Gratzki, A., Hollmann, R., & Behr, H. (2009). The CM-SAF operational scheme for the satellite based retrieval of solar surface irradiance — A LUT based eigenvector hybrid approach. *Remote Sensing of Environment*, *113*(5), 1012–1024.

Ohmura, A., Dutton, E. G., Forgan, B., Fröhlich, C., Gilgen, H., Hegner, H., et al. (1998). Baseline Surface Radiation Network (BSRN/WCRP): New precision radiometry for climate research. *Bulletin of the American Meteorological Society*, *79*, 2115–2136.

Perez, R., Aguiar, R., Collares-Pereira, M., Dumortier, D., Estrada-Cajigal, V., Gueymard, C., et al. (2001). Solar resource assessment: A review, in solar energy — The state of the art. *ISES Position Papers* (pp. 497–562). London: James & James Science Publishers1 902916239.

Perez, R., Seals, R., & Zelenka, A. (1997). Comparing satellite remote sensing and ground network measurements for the production of site/time specific irradiance data. *Solar Energy*, *60*, 89–96.

Posselt, R., Mueller, R. W., Stöckli, R., & Trentmann, J. (2012). Remote sensing of solar surface radiation for climate monitoring — The CM-SAF retrieval in international comparison. *Remote Sensing of Environment*, *118*, 186–198.

Razykov, T. M., Ferekides, C. S., Morel, D., Stefanakos, E., Ullal, H. S., & Upadhyaya, H. M. (2011). Solar photovoltaic electricity: Current status and future prospects. *Solar Energy*, *85*, 1580–1608.

Rigollier, C., Levefre, M., & Wald, L. (2004). The method Heliosat-2 for deriving shortwave solar radiation from satellite images. *Solar Energy*, *77*, 159–169.

Shi, Y., & Long, C. N. (2002). Techniques and methods used to determine the best estimate of radiation fluxes at SGP central facility. In D. Carrothers (Ed.), *Proceedings of the Twelfth ARM Science Team Meeting*. Richland, WA: U.S. Department of Energy.

Sneep, M., de Haan, J. F., Stammes, P., Wang, P., Vanbauce, C., Joiner, J., et al. (2008). Three-way comparison between OMI and PARASOL cloud pressure products. *Journal of Geophysical Research*, *113*, D15S23, http://dx.doi.org/10.1029/2007JD008694.

Stammes, P., Sneep, M., de Haan, J. F., Veefkind, J. P., Wang, P., & Levelt, P. F. (2008). Effective cloud fractions from the Ozone Monitoring Instrument: Theoretical framework and validation. *Journal of Geophysical Research*, *113*, D16S38, http://dx.doi.org/10.1029/2007JD008820.

Veefkind, J. P., Aben, I., McMullan, K., Förster, H., de Vries, J., Otter, G., et al. (2012). TROPOMI on the ESA Sentinel-5 precursor: A GMES mission for global observations of the atmospheric composition for climate, air quality and ozone layer applications. *Remote Sensing of Environment*, http://dx.doi.org/10.1016/j.rse.2011.09.027.

Wang, P., Stammes, P., & Mueller, R. (2011). Surface solar irradiance from SCIAMACHY measurements: Algorithm and validation. *Atmospheric Measurement Techniques*, *4*, 875–891, http://dx.doi.org/10.5194/amt-4-875-2011.

Wang, P., Stammes, P., van der A, R., Pinardi, G., & van Roozendael, M. (2008). FRESCO+: An improved O_2 A-band cloud retrieval algorithm for tropospheric trace gas retrievals. *Atmospheric Chemistry and Physics*, *8*, 6565–6576, http://dx.doi.org/10.5194/acp-8-6565-2008.

Wielicki, B.A., Barkstrom, B. R., Harrison, E. F., Lee, R. B., III, Smith, G. L., & Cooper, J. E. (1996). Clouds and the Earth's Radiant Energy System (CERES): An earth observing system experiment. *Bulletin of the American Meteorological Society*, *77*, 853–868.

Willmott, C. J. (1982). Some comments on the evaluation of model performance. *Bull. Amer. Meteor. Soc.*, *63*, 1309–1313.

Yan, H. R., Huang, J. P., Minnis, P., Wang, T. H., & Bi, J. R. (2011). Comparison of CERES surface radiation fluxes with surface observations over Loess Plateau. *Remote Sensing of Environment*, *115*, 1489–1500.

Zelenka, A., Perez, R., Seals, R., & Reme, D. (1999). Effective accuracy of satellite-derived hourly irradiances. *Theoretical and Applied Climatology*, *62*, 199–207.

Zhang, Y. -C., Rossow, W. B., Lacis, A. A., Oinas, V., & Mishchenko, M. I. (2004). Calculation of radiative fluxes from the surface to top of atmosphere based on ISCCP and other global data sets: Refinements of the radiative transfer model and the input data. *Journal of Geophysical Research*, *109*, D19105, http://dx.doi.org/10.1029/2003JD004457.

Zhang, Y., Rossow, W. B., & Stackhouse, P. W., Jr. (2006). Comparison of different global information sources used in surface radiative flux calculation: Radiative properties of the near-surface atmosphere. *Journal of Geophysical Research*, *111*, D13106, http://dx.doi.org/10.1029/2005JD006873.